Mine Water and the Environment (2022) 41:428–436
https://doi.org/10.1007/s10230-022-00870-x

TECHNICAL ARTICLE

An Analog Model Study on Water–Sand Mixture Inrush Mechanisms During the Mining of Shallow Coal Seams

Yifan Zeng[1,2,3] · **Huiqing Lian**[2] · **Xin Du**[1] · **Xianfeng Tan**[3] · **Demin Liu**[2]

Received: 24 March 2021 / Accepted: 13 April 2022 / Published online: 7 May 2022

Abstract

Water–sand mixture inrushes into shallow underground workings have caused casualties and property loss. A coupled fluid–solid analog model was developed to simulate the water–sand mixture inrush processes during mining from fracture production and development, based on the hydrogeological conditions at the #22304 working face of the Shigetai coal mine in the Erdos coal basin of northeast China. The deformation characteristics of the overlying strata and water pressure variations within the water-flowing fractured zone were monitored and analyzed. The results show that the water–sand mixture inrush consists of three stages: development of cracks in the overlying strata, initiation of a water inrush channel, and evolution of the inrush channel. The stresses of the overlying strata, water pressures, and permeability characteristics of water and sand inrush pathways change within the three stages. These findings lay a solid foundation for predicting water–sand mixture inrushes in shallow coal mines.

Keywords Water and sand inrush · Water pressure · Lithologic association · Water–rock coupling · Fissure · China

Introduction

The Shendong coal mining area, located in the Erdos coal basin of northeast China, a contiguous area of the Mu Us Desert and the Loess Plateau, is the largest coal production base in the world, having reached 200 million t/a (Zhou et al. 2015). The surface of the Shendong mining area is covered by a thick Cenozoic loose gravel layer. Precipitation recharges this gravel layer, forming a medium—strong aquifer. The coal seam in this section is less than 150 m below the surface. Mining is prone to water–sand mixture inrushes because the bedrock between the coal seam and the overlying aquifer is as thin as 1.4 m, making it easy for mining-induced fractures to connect to the overlying porous-medium aquifer. When the total collapse mining method is applied to a fully mechanized working face, the risk of a water–sand mixture inrush is especially high. In 1990, roof collapses occurred twice during the tunneling process in the Ciyaowan coal mine, causing water–sand inrush accidents and a loss of 2,000 m of roadway. In 1993, a water–sand inrush occurred at the #1203 working face of the Daliuta coal mine (Wu et al. 2006; Zeng et al. 2016), in which the fully mechanized working panel was flooded, and 19 days of production was lost. In 2001, a large-scale water–sand inrush occurred during tunneling of the Shangwan Coal Mine I because of a roof collapse (LaMoreaux et al. 2014). From 2008 to 2009, the Shigetai coal mine had three water–sand inrush accidents. In 2010, a water–sand inrush occurred in the #22402 fully mechanized mining face of the Halagou coal mine through faults (Wu et al. 2015; Zeng et al. 2017).

In dealing with a water–sand inrush in a shallow Jurassic coal seam in northern Shaanxi province, Xu (2008) found that sand had self-healing properties during the flow process and proposed that the outlet diameter of the funnel was the key factor for sandy soil stability. Zhang (2008) calculated the height of the hydraulic-conductive fractured zone for

✉ Yifan Zeng
zengyifan_1011@sina.com

[1] National Engineering Research Center of Coal Mine Water Hazard Control, University of Mining and Technology, Beijing 100083, People's Republic of China

[2] Hebei State Key Laboratory of Mine Disaster Prevention, North China Institute of Science and Technology, Yanjiao 101601, China

[3] Engineering Innovation Center of Restoration and Reclamation in Mining-Induced Subsidence Land, Ministry of Natural Resources, Jining 272000, Shandong, China

fully mechanized coal mining using the multiple regression theory and the hydraulic head of the aquifer as the water inrush criterion. Zhang (2017) provided analyses of water-inrush identification and a simulation modelling prediction work based on the multi-element fitting formulas and the stress and fluid flow coupled system module of finite difference software FLAC3D. According to Sui (2008), the initial water head and fissure width of the flow path are the key factors controlling a water inrush discharge at the working face of a coal mine. Yang (2008) discussed how pore water pressure changes as a water and sand mixture migrates. Wang (2009) established the critical condition and prediction formulas for preventing a water–sand inrush when the critical hydraulic gradient is caused by permeability. Sui (2007) established a discrimination method based on the stress condition of the aquifer during the water inrush process to calculate the critical hydraulic gradient of a roof water burst and determined that water under the desert pavement plays a key role in controlling the local ecological environment.

Recent research on water inrushes in shallow coal mines involving sediment have mainly been based on field measurements (Li et al. 2017; Zhang et al. 2005), physical simulations (Huang et al. 2019; Zha et al. 2020), numerical simulations (Chen et al. 2016; Jin et al. 2021), and theoretical analysis (Sui et al. 2015). However, no systematic research has been conducted on the necessary conditions for water–sand inrush, i.e. the caving processes of the overlying strata in shallow coal seams and how the fractured zone changes with stresses. We used a coupled fluid–solid physical simulation to investigate and analyze the deformation pattern of the overlying strata and variations of water pressure within the fractured zone. The permeability and transformation of water–sand inrush channel were characterized at different stages of coal seam roof collapse and the relationships between transport channels, water–sand mixtures, and mining disturbance were analyzed. The research results provide an empirical basis for shallow coal mining under aquifers to ensure safe mining, while also minimizing environmental damage.

Experiment Prototype

The #22304 working face of the Shigetai coal mine in the Shendong mining area was taken as the prototype of this physical simulation test. The mine is located in Ulan Mulun Hedong north, ≈ 55 km northwest of Shenmu County in Shaanxi province. The Shendong mining area is located in the area between the Mu Us Desert and the Loess Plateau. The overall topography is undulating with topographic highs in the mid-east and lows in the west. The lowest point is located in the Ulan Mulun River Valley at 1,122 m above mean sea level (amsl), whereas the highest point is in the north of the mine at an elevation of 1,351.4 m amsl. Most of the mine area is covered by sand: undulating dunes and flat sand with sparse surface vegetation and intermittently exposed bedrock on both sides of the valley.

The working face of the 2–2 coal seam is located in the 3rd panel. The coal seam is 3–3.5 m thick and has a dip angle of 1–3°. The ground elevation is between 1,255 and 1,290 m amsl. The floor level is 1,170–1,198 m amsl. The area of the working face is 573,701 m^2 (2,433 m long and 235.8 m wide).

Water Source

Atmospheric precipitation is the indirect source of water to the mine. The fissured phreatic aquifer (J2z) of #22,304 working face is ≈ 15—20 m thick and weak in water storage. The fractured confined aquifer (J1-2z) in the lower Jurassic Yanan formation is ≈ 90–250 m thick. The water-bearing and aquitard layers alternate. The vertical recharge is poor, and there is little water enrichment. This formation can be considered as relative impermeable, and does not pose a threat to mining.

The phreatic aquifer (Q3s) in the Salawusu formation is thicker, with a maximum of 40.3 m. The aquifer structure is porous and easily recharged by atmospheric precipitation. The aquifer is rich in water storage and the direct water recharge source for the #2 coal seam. Although the average annual rainfall in this area is only 435.7 mm, the precipitation is concentrated in July through September (≈ 60–70% of the total annual precipitation), and certainly influences mining during this time period.

Water Pathway

Based on the degree of failure of the strata overlying the goaf, three zones are present: caving zone, fractured zone, and bending zone. Water can be introduced into the mine if the fractured zone connects to an overlying water body or aquifer. The caving and fractured zones provide pathways for flowing water.

The coal seam is 3–3.5 m thick in the Shigetai coal mine and the roof consists of sandstone and siltstone. The uniaxial compressive strength is generally 2,040 MPa, which is classified as medium-hard rock. According to the "calculation method for buildings, water, railway and main roadway of coal pillar and coal mining regulations" (Wu et al. 2013), the maximum height of the water-flowing fracture zone can be calculated by Eq. (1):

$$H_{li} = 20\sqrt{\sum M} + 10 \quad (1)$$

where M is the mining thickness. The calculated height ranges from 41.3 to 43.6 m, which exceeds the maximum bedrock thickness (≈ 38 m) that overlies coal seam 2–2. This suggests that the water-flowing fractured zone will likely reach the Quaternary loose sand layer aquifer, resulting in the flow of water and sand from the loose layer into the working area.

Water-Filling Intensity

Water inflow is mainly related to the thickness and lithology of the bedrock, the aquifer's thickness and degree of water abundance, rainfall intensity, and the mining and tunneling method. In the paleo-topographic low areas, the overlying bedrock is very thin, and the aquifer is relatively thick. The water abundance is generally strong. When the working face is under this section, the risk of water–sand inrush may be higher. On the other hand, in the paleo-topographic high areas where the overlying bedrock is thicker and the aquifer is thinner, the water richness is weak. Water filling is less intense when the working face is under this section; water inflow is mainly caused by the nature of the caving and water-flowing fractured zones and the water released from the aquifer. During the rainy season, rainfall rapidly recharges the groundwater and enters the aquifer through the water-flowing fractured zone, thus increasing the water-recharge strength.

Materials and Method for a Coupled Fluid–Solid Simulation

Simulation Material

The primary difficulty in a coupled fluid–solid analog simulation is determining the water resistance of impermeable materials used for the aquifuge. Based on previous research, materials that can be used for the aquifuge are: loess, sand, clay, silicone oil, Vaseline, barite powder, talc powder, solid paraffin, and hydraulic oil. The mechanical properties and water resistance of the materials are different due to the different combinations and proportions of the selected materials. Testing was conducted to determine the material compositions comparable to the field strata, and to meet the strength, deformation and water resistance requirements in the analog modeling processes.

According to the lithologic column of the Shigetai Mine (Fig. 1), the strata typically consists of sandstone, sandy mudstone, siltstone, fine sandstone, and the coal seam. A total of five solid phase simulation experiments were designed. The material compositions of each stratum are presented in Table 1.

Material Testing

The compressive strength, immersion, permeability, water absorption, and tensile strength were tested to select the most appropriate materials. The test apparatus was a cylindrical mold, 50 mm in diameter and 100 mm tall.

According to the ratio of the five formation materials, 0%, 5%, 8%, and 10% paraffin wax were respectively added as a cementing agent. The compressive strength of the samples was measured for specimens of different proportions by a uniaxial compressive strength test after natural curing for seven days. The influence of the different paraffin contents on the compressive strength is shown in supplemental Fig. S-1.

Compressive Strength Test

The compressive strength test was conducted for another group of materials with Vaseline and paraffin ratios at 3%,

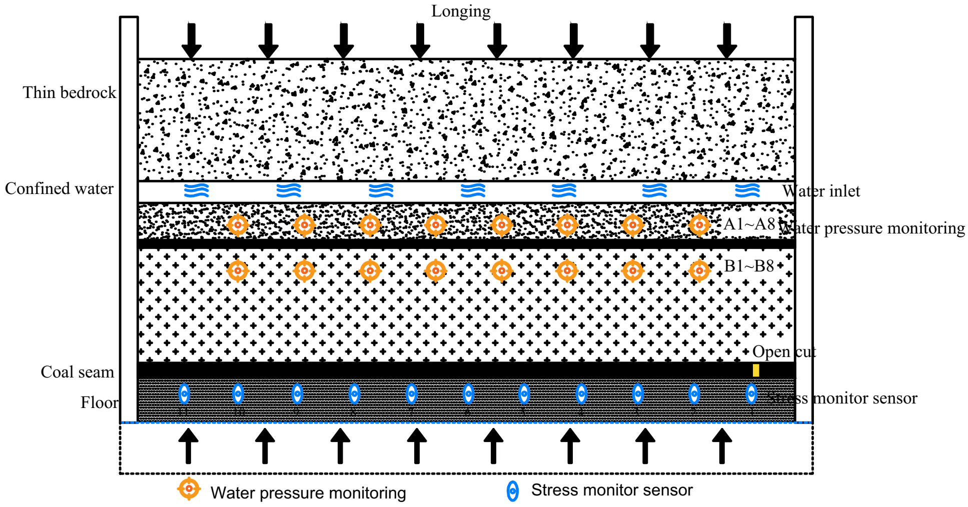

Fig. 1 Lithology of the study area

Table 1 Lithologic composition in layers

Stratum	Ratio of sand: carbonate: gypsum	Density (g/cm^3)
Medium sandstone	7: 3: 7	2.27
Sandy mudstone	7: 6: 4	2.38
Siltstone	7:5: 5	2.35
Coal	9: 7: 3	1.31
Fine sandstone	7:4:6	2.31

5%, and 8%. The specimen samples were tested after seven days. The influence of different paraffin contents on the compressive strength is shown in supplemental Fig. S-2. A total of 35 groups of uniaxial compressive strength tests were completed.

Immersion Test

The paraffin content combinations were 5%, 8%, and 10%. The uniaxial compressive strength test was conducted 24 h after the specimens were put in the water. A total of 20 groups of immersion tests were completed. The results are shown in supplemental Fig. S-3.

Permeability Test

The sample diameter was 2.5 cm after sample preparation. The sample was placed in the mold and tested for permeability after three days. After the conversion calculation, the permeability value was obtained, and then the influence of paraffin on the permeability coefficients of different similar materials was obtained (supplemental Fig. S-4). A total of 35 groups of permeability tests were completed.

Water Absorption Experiment

The amount of paraffin in the material ranged from 5 to 8%. After sample preparation, the specimens were weighed at the height of the upper and lower parts after seven days of natural maintenance. The specimen was immersed for 24 h, during which the quality of the specimen was measured every 2 h to test its water absorption. A total of five samples were made and 60 effective data points were acquired. The relationship between water absorption and time is shown in supplemental Fig. S-5.

Tensile Strength Test

The tensile strength represents the maximum uniform plastic deformation resistance of materials. The deformation of the tensile specimen was uniform before the maximum tensile stress was reached, but beyond the maximum tensile stress, the specimen began to show necking, which produces concentrated deformation. For brittle material without (or with very small) uniform plastic deformation, the tensile strength reflects the material's fracture resistance. The influence of paraffin content on the tensile strength of the materials is shown in supplemental Fig. S-6.

According to the experimental results of the different proportioning schemes, the mechanical characteristics and water resistance of the similar materials were obtained at different ratios. This provided the basis for the determination of similar material proportioning schemes for different types of water-resistant layers. Table 2 summarizes the simulation experiment schemes with various proportions of similar materials.

The Simulation Test Process

Model Setup

The model test rig adopts a self-developed physical simulation system of solid–liquid coupling coal seam mining. The main part of the test system is composed of a mine pressure simulator (Fig. 2) and an automatic water injection system for the aquifer. The auxiliary part is composed of sensors for monitoring of strata displacement and system of stress / water pressure, an oven, a heating mixer, and a high speed camera.

According to the special engineering geological conditions in the #22304 working face and the solid–liquid two-phase test specifications, the analog model of this experiment was scaled at 1:100. The dimensions are 2,000 mm long, 300 mm wide, and 1,800 mm high. The simulated material was selected according to the material test results. The model block was made up of layers, with the upper part simulating the loose aquifer and the lower the overlying bedrock. In the aquifer thickness portion, the sand was saturated with water and placed directly on the bedrock surface (Fig. 2). A measuring line was laid along the landscape orientation of the coal seam floor, with 11 YHD-50 resistive displacement sensors. The water pressure sensors were divided into two lines along the aquifer, with eight in each layer (16 in total).

Test Process

First Collapse of the Main Roof

The open cut began 20 cm from the model boundary, equivalent to 20 m of reserved coal pillar. The length of the open cut was 8 cm. When the face advanced to 33 m, fractures appeared in the overlying strata and the immediate roof began to bend. As the face was pushed to 38 m, the initial

Table 2 Material compositions for simulation experiment

Lithology	Model thickness (cm)	Hierarchy number	Proportioning number	Sand per layer (kg)	Calcium carbonate per layer (kg)	Plaster amount per layer (kg)	Per layer of water (kg)	Paraffin per layer (kg)	Each layer of Vaseline (kg)
Aeolian sand	18.35		982						0
Mudstone	17.15	12	873	12.01	1.2	0.51	1.52	0.6	0
Medium sandstone	8.5	4	855	17.85	1.28	1.28	2.27	0.89	0
Sandy mudstone	4.9	5	882	8.23	0.94	0.24	1.05	0.41	0
Siltstone	9.9	4	764	20.37	2.04	1.36	2.64	1.02	0
Medium coarse-grained sandstone	14.15	7	855	16.98	1.21	1.21	2.16	0.85	0.85
1# coal	0.4	1	982	3.41	0.34	0.09	0.43	0.17	0.17
Siltstone	2.91	1	773	23.95	2.79	1.2	3.1	1.2	1.2
1# coal	2.3	3	982	6.54	0.65	0.16	0.82	0.33	0.33
Sandy mudstone	4.38	4	882	9.2	1.05	0.26	1.17	0.46	0.46
Siltstone	19.24	10	773	15.83	1.85	0.79	2.05	0.79	0.79
Fine sandstone	6.2	3	764	17.01	1.7	1.13	2.2	0.85	0.85
Siltstone	9.01	5	773	14.83	1.73	0.74	1.92	0.74	0.74
Sandy mudstone	1.9	2	882	7.98	0.91	0.23	1.01	0.4	0.4
2# coal	3.51	1	982	29.95	3	0.75	3.74	1.5	0
Sandy mudstone	6.6	3	882	18.48	2.11	0.53	2.35	0.92	0
Fine sandstone	3.4	1	764	27.98	2.8	1.87	3.63	1.4	0

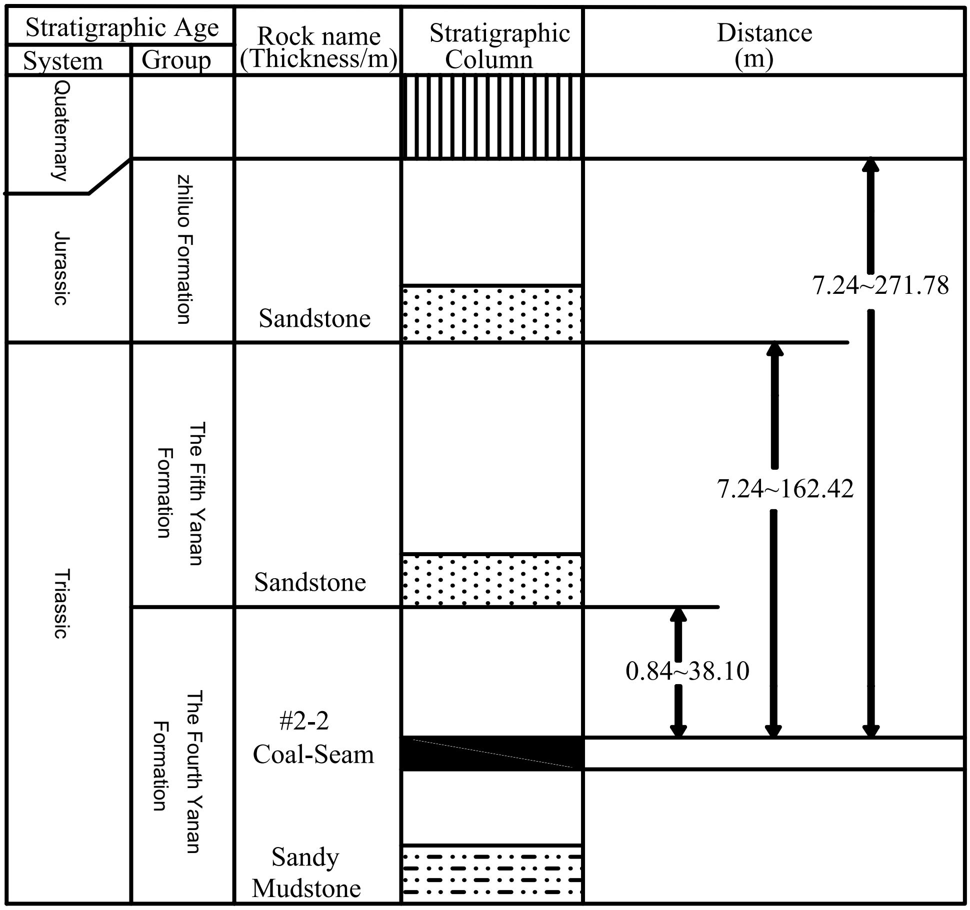

Fig. 2 Mine pressure simulator model

collapse occurred, and the block structure of the rock was obvious. The maximum rock mass was 12.2 m, and the collapse rock height was 1.9 m. The immediate roof rock was bent and fractured. In the goaf area, the fractures split the immediate roof rock into two unequal fractured rock masses, with horizontal micro-fractures in the upper strata.

As the working face continued to advance, the immediate roof separated both horizontally and vertically. The lower fault strata gradually expanded under the overlying load to form a cantilever beam structure. The immediate roof fell again as the mining reached 48 m. The lower strata of the main roof in the 2 m range of the coal seam continuously collapsed. The collapse shape was a flat arch, with a 34 m span length of flat arch and caving angle of 65°. The immediate roof strata continued to collapse (supplemental Fig. S-7).

Initial Collapse of the Main Roof

As the working face advanced to 53 m, the immediate roof continued to expand along the horizontal bedding and slowly collapsed as a cantilever structure. At the same time, separation fracture occurred in the lower 18 m range of the main roof strata, and the separation fracture continued upward as the work surface continued to be advanced. Because of the subsidence of the roof rock, the immediate roof was falling down continuously. When the face reached the equivalent of 63 m, the overlying strata exhibited a large range of deformation and destruction, resulting in the first collapse of the main roof. The collapse began at 53 m, as a gentle arch. The horizontal span at the top of collapse was 38 m. The rock burst angle was 60°. At the same time, the horizontal fracture developed to 22 m from the top of the coal seam. The initial roof collapse was behind the working face and occurred relatively quickly. There was a clear separation zone between the fractured zone and the overlying strata when the main roof collapsed for the first time. The strata above the separation zone only exhibited bending deformation. When the lower strata were connected by vertical growth fissures, the main roof collapsed, as shown in supplemental Fig. S-8.

As the working face advanced the equivalent of 73 m, the roof started to collapse periodically. The caving distance was 12 m. As the damage progressed to 45 m above the coal seam, the whole fracture zone was six times the mining height. The maximum gap between the roof rock and the falling body was 0.5 m. The horizontal span of the collapse was 50 m. The rock burst angle was 60°. The gap was closed below 34 m above the coal seam when the interlayer horizontal fracture developed to the top of the coal seam at 43 m. The periodic collapse of the roof is shown in supplemental Fig. S-9.

By the time that the working face had advanced the equivalent of 88 m, the roof had collapsed three times. The caving length was 12 m. As the damage progressed to 46 m above the coal seam, the horizontal fractures grew to 55 m above the seam and formed a large separation space. At 116 m, the roof had collapsed three times. The gap extended to 0.5 m at 55 m above the seam. The horizontal collapse span reached 44 m and formed a separation space. When the horizontal fracture between the layers reached 74 m above the coal seam, the height of the caving zone was 10 times the mining height. The collapse of the roof in the third cycle is shown in Fig. S-9.

Collapse of the Caving Rock Layer

By the time the working face had advanced 143 m, the roof had collapsed seven times. The caving length was 16 m. Fractures developed to 94.5 m above the coal seam, so the height of the fracture zone was 12.6 times that of the coal seam. The separation space between the flexural rock layer and the broken rock formation on the upper part of the roof had closed. The separation space between the collapsed strata 60 m above the roof suddenly increased. Surface subsidence was obvious. At the junction of the working face and the coal wall, there were two obvious fracture cracks extending diagonally above the roof. The caving angle was 58°. The top slate above the working face collapsed. The separation layer fissure is shown in Fig. S-10.

As the face reached 153 m, the main roof dramatically collapsed, producing stair-stepped ground subsidence. There were only two zones instead of the traditional "upper three zones". The height of the fracture zone was 16.4 times the mining height. There were two fracture cracks at 3 m behind the cutting hole of the coal wall and the working face, which directly affected the surface. The rock collapse angle was 62° at the open-off cut, and the rock collapse angle was 60° at the topping line. supplemental Fig. S-10 shows the overlying cutting collapse. Detailed data of the first and periodic collapses are shown in Table 3.

Analysis of Test Results

The analog simulation experiments provided a unique visual research method. First, the coupled solid–liquid simulation experiment was realized when the water head was regulated according to hydraulic heads in the simulated aquifer. Second, the experimental results reproduced the complete process of fracture development through water inrush to sand inrush, clearly demonstrating the mechanisms of roof failure and water–sand mixture inrush.

Table 3 Data of the first and periodic stress of roof

Name	First weighting	Periodic pressure								Periodic average
		1	2	3	4	5	6	7	8	
Step (m)	53	11	9	14	16	13	16	11	10	12.5
Caving angle (degree)	75	65	72	70	70	60	73	70	65	68.12
Fissure angle (degree)	70	82	58	62	45	50	49	45	49	55

Fracture Development in the Overlying Strata

As the working face advanced from 8 to 38 m, there was no sharp change either in floor stress or monitored water pressure, but gradual changes were observed. The first measuring point showed that the stress beneath the coal seam at both sides of the open-off cut increased. The second point showed that the stress began to diminish as the working face was advanced beyond 10 m. When it reached 58 m, the stress at the fourth measuring point increased, and reached its maximum of 0.486 MPa when the working face reached 78 m. As the working face was extended up to 78, the stress at the fifth measuring point began to increase. It was shown by monitoring of the floor stress was rising as the working face moved forward. At the same time, the stress at the bottom of the goaf began to decrease and stress unloading began (supplemental Fig S-11).

There was no change at the top of the cutting hole until the working face was moved from 38 to 78 m, when the pore water pressure at sensors a-2, a-3, and a-4 located below the aquifer began to increase. However, the water pressure changed little at other measure points. Between 74 and 140 m, the water pressure began to show an overall rising trend with fluctuations. The pore water pressure began to decrease as the working face extended beyond 140 m (Fig. 3).

As the working face advanced to 88 m, the third periodic roof collapse occurred. Fractures still continued to communicate and expand within the fault zone in the horizontal direction, though the floor stress curve fluctuated relatively little. At measuring points 06, 07, 08, and 09, stresses increased as the working face advanced, while stresses at points 01 through 05 were stable. It could be inferred that the floor failure depth had peaked in the early stage of working face advancement and would no longer develop downward. Observations at the front of the model indicated that the right fissure at the bottom interface of floor of the stope had developed to the bottom of the aquifer and had an upward trend (supplemental Fig. S-12).

As the working face moved from 103 to 113 m, only sensors a6 and a1 (located in the upper part of the working face) measured water pressure fluctuations (Fig. 4). Overburden failure was serious. Cracks increased and continued to expand and communicate. The overlying strata were largely destroyed, and the cracks increased and continued to expand and communicate with each other.

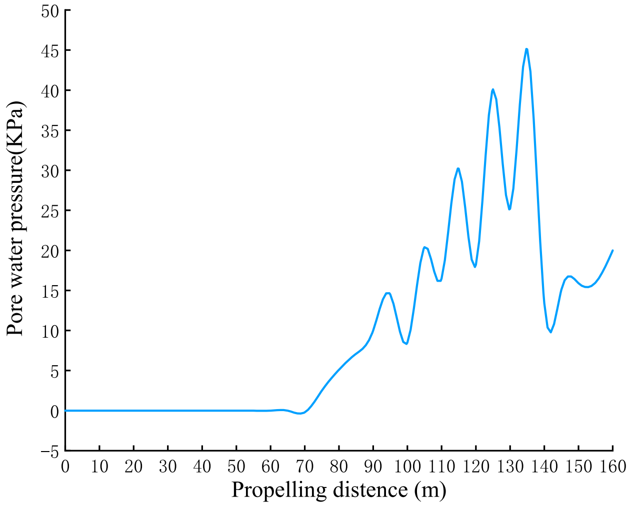

Fig. 3 Pore water pressure over cutting face at sensor 3

At 123 m, the first water inrush appeared ≈ 30 m behind the working face under the aquifer. The increased water inflow further exacerbated fracture development within the bedrock below the aquifer (supplemental Fig. S-13). As the working surface continued to move forward, the floor pressure monitoring points in the middle zone remained in a state of decompression. The pore water pressure measured at points A1, B1, A6, and B6 below the aquifer on both sides of the coal wall increased (Fig. 5). Water flow in the fissure increased in response to the amount of water. Quartz sand and similar simulated material in the aquifer were continuously flushed out of the model as the water inflow as the fracture channel became progressively greater.

At 30 m from the stop line, the overlying fissure was no longer inclined upward at 35 m distance from the bottom floor, but vertically upwards, forming a fissure channel (supplemental Fig. S-14). The water–sand inrush broke through the fissure channel at a rate of 1 L/min. The localized burst of water and sand grew as the water inrush channel expanded and evolved, and the number of inrush points continuously grew, which enhanced the overall effect. Water, sand, and rock fragments flowed

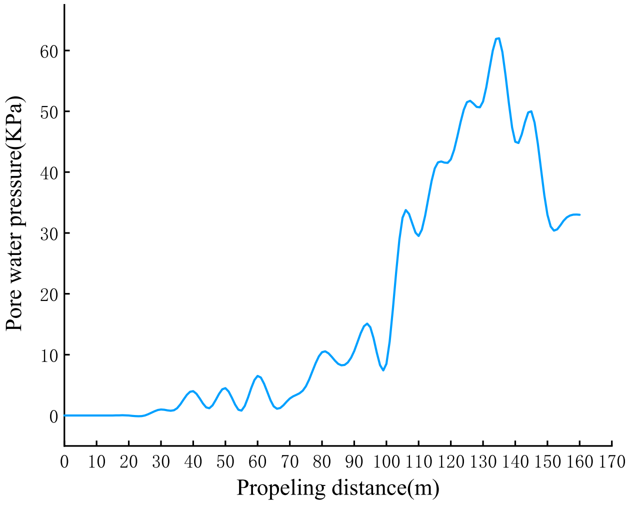

Fig. 4 Pore water pressure at A6 sensor

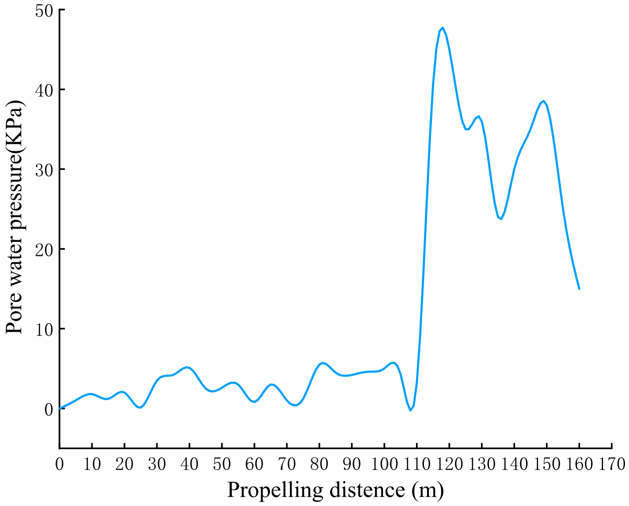

Fig. 5 Pore water pressure at B6 sensor

out together, eventually evolved into a roof water–sand inrush disaster.

Conclusion

Based on the results of the water resistance experiment, the selected materials in the analog model matched the lithology of the #22304 working panel of the Shigetai coal mine. The strength, deformation, and water resistance met the requirements of analog modeling. Visual observations and monitoring data indicate that the water–sand inrush followed the following steps: fracture production, fracture development, fracture evolution, water inrush, and finally sand inrush.

The stress and water pressure of the rock cover changed regularly during the different stages of the water–sand inrush events, though the distances over which the different stages developed would be different in another mine. There was no sharp change in the stress of the floor or monitoring water pressure as the working face advanced from the equivalent of 8 to 38 m. The zone of the floor under stress grew in size as the working face advanced, though the stress of the mined out area's floor began to decrease as pressure was relieved. As the working face advanced from 38 to 78 m, the pore water pressure began to change under the aquifer. The water pressure fluctuated upward after the face advanced from 74 to 140 m. The pore water pressure dropped sharply after that.

The water inrush channel initiation stage began as the working face advanced to 88 m. After the roof had periodically collapsed three times, the roof collapsed again, and cracks continued to grow and communicate with each other. A fissure on the bottom of the stope rose to just below the aquifer, causing the water pressure to fluctuate from top to bottom. The mining-induced fracture was on the brink of communicating with the roof aquifer.

Once the fissure channel penetrated the aquifer, the water and sand migration began. The water inrush channel began evolving when the working face advanced to 123 m. The water inrush first appeared at the bottom of the aquifer about 30 m behind the mine face and then the water quantity continuously increased. Fissure development in the bedrock beneath the aquifers was intensified by erosion. With more water in the fissure and more water pressure, the water inflow in the fracture channel increased, incorporating the sand and roof material together. Finally, the overlying rock fissure formed a vertical fissure channel 35 m below the slab. The water–sand inrush broke through the fissure channel at a rate of 1 L/min. The localized burst of water and sand grew as the water inrush channel expanded and evolved, the number of inrush points continuously grew, which enhanced the overall effect. Water, sand, and rock fragments flowed out together, eventually evolved into a roof water–sand inrush disaster.

Supplementary Information The online version contains supplementary material available at https://doi.org/10.1007/s10230-022-00870-x.

Acknowledgements This research was financially supported by China's National Natural Science Foundation (grants 42072284, 42027801), Fundamental Research Funds for the Central Universities (grant 3142017064), and the Open Fund of the Hebei State Key Laboratory of Mine Disaster Prevention (grant KJZH2016K01).

References

Chen L, Feng X, Xie W, Wen Z, Zheng Z (2016) Using a fluid–solid coupled numerical simulation to determine a suitable size for barrier pillars when mining shallow coal seams beneath an unconsolidated, confined aquifer. Mine Water Environ 36(1):1–11. https://doi.org/10.1007/s10230-016-0404-6

Huang Q, He Y, Cao J (2019) Experimental investigation on crack development characteristics in shallow coal seam mining in China. Energies. https://doi.org/10.3390/en12071302

Jin Z, Peng T (2021) Control of the internal and external staggered distance of coal mining face to the water-conducting fissures in the overlying strata of the near coal. Adv Civ Eng. https://doi.org/10.1155/2021/1499675

LaMoreaux JW, Wu Q, Zhou W (2014) New development in theory and practice in mine water control in China. Carbonate Evaporite 29:141–145. https://doi.org/10.1007/s13146-014-0204-7

Li J, Liu C (2017) Formation mechanism and reduction technology of mining-induced fissures in shallow thick coal seam mining. Shock Vib 2017(pt 3):1–14. https://doi.org/10.1155/2017/1980817

Sui W, Dong QH (2008) Variation of pore water pressure and its precursor significance for quicksand disasters due to mining near unconsolidated formations. Chin J Rock Mech Eng 27(9):1908–1916. https://doi.org/10.1016/S1872-5791(08)60057-3 ((**in Chinese**))

Sui W, Cai GT, Dong QH (2007) Experimental research on critical percolation gradient of quicksand across overburden fissures due to coal mining near unconsolidated soil layers. Chin J Rock Mech Eng 26(10):2084–2091. https://doi.org/10.1016/S1872-2067(07)60020-5(inChinese)

Sui W, Hang Y, Ma L et al (2015) Interactions of overburden failure zones due to multiple-seam mining using longwall caving. B Eng Geol Environ 74(3):1019–1035. https://doi.org/10.1007/s10064-014-0674-9

Wang SD, Shen XH, Mou P (2009) Perdition of sand and water inrush in seam with shallow depth and under rich water aquifer in Hanjianwan mine. Coal Sci Technol 01:92–95

Wu Q, Wang M (2006) Characterization of water bursting and discharge into underground mines with multi-layered ground-water flow systems in the north China coal basin. Hydrogeol J 14(6):882–893. https://doi.org/10.1007/s10040-006-0021-8

Wu Q, Zhao SQ, Dong SN Li JS (2013) Coal mine water prevention manual. Coal Industry Press, pp 652–678 **(in Chinese)**

Wu Q, Lin Y, Zhou W, Li B, Zhao B, Lin S, Sun W, Zeng Y (2015) Evaluation of water inrush vulnerability from aquifers overlying coal seams in the Menkeqing coal mine, China. Mine Water Environ 34:258–269. https://doi.org/10.1007/s10230-014-0313-5

Xu YC (2008) Fluidity test on sand blended with clay. J Chin Coal Soc 33(5):496–499. https://doi.org/10.3901/JME.2008.05.160

Yang W, Sui W, Xia X (2008) Model test of the overburden deformation and failure law in close distance multi-seam. Mining J Coal Sci Eng (China) 14(2):181–185. https://doi.org/10.1007/s12404-008-0037-x

Zeng Y, Wu Q, Liu S (2016) Vulnerability assessment of water bursting from Ordovician limestone into coal mines of China. Environ Earth Sci 75(22):1431. https://doi.org/10.1007/s12665-016-6239-4

Zeng Y, Wu Q, Liu S (2017) Evaluation of a coal seam roof water inrush: case study in the Wangjialing coal mine. China Mine Water Environ Sci 37(1):174–184. https://doi.org/10.1007/s10230-017-0459-z

Zha H, Liu W, Liu Q (2020) Physical simulation of the water-conducting fracture zone of weak roofs in shallow seam mining based on a self-designed hydromechanical coupling experiment system. Geofluids 8:1–14. https://doi.org/10.1155/2020/2586349

Zhang J, Peng S (2005) Water inrush and environmental impact of shallow seam mining. Environ Geol 48(8):1068–1076. https://doi.org/10.1007/s00254-005-0045-8

Zhang Y, Zhang H, Chen P (2008) Visual exploration of fissure field of overburden and rock. J China Coal 33(11):1216–1219. https://doi.org/10.1002/clen.200700058(inChinese)

Zhang J, Yang T, Wang B, Zhao Q, Liu D, Ren Y (2017) Prediction analysis of roof water-inrush in shallow coal seam with surface valley runoff. J Min Safe Eng 34(5):868–875. https://doi.org/10.13545/j.cnki.jmse.2017.05.007